The Stokes drift and wave induced-mass flux in the North Pacific

Hitoshi Tamura[1], Yasumasa Miyazawa[1], Lie-Yauw Oey[2]

1 Research Institute for Global Change, Japan Agency for Marine-Earth Science and Technology, Yokohama, Kanagawa, Japan

2 Program in Atmospheric and Oceanic Sciences, Princeton University, Princeton, NJ, USA

htamura@jamstec.go.jp

Abstract

Stokes drift and wave induced-mass flux in realistic wave fields and ocean currents in the North Pacific Ocean are studied using a third generation wave model with ambient geostrophic currents estimated from satellite altimetry data to directly estimate the Stokes drift for random directional waves. Comparison with *in situ* buoy data shows that the model performed well in representing the Stokes drift field and total wave momentum. In the North Pacific, the annual mean surface Stokes drift ranges from 2 to 10 cm/s and the mean Stokes *e*-folding depth is 1 to 2 m. The Stokes drift fields estimated using bulk wave parameters compare poorly against buoy data, and are shown to overestimate

(underestimate) the Stokes *e*-folding depth (the surface Stokes drift) computed directly from wave spectra by as much as 5-20 times larger (2-10 times smaller). The spatial distributions of mean wave height and mass transport approximately follow the synoptic scale associated with atmospheric forcing, and the divergence of wave induced-mass flux is significantly modified by local fetch, the coast and ocean currents. Due to strong wave refraction along the Kuroshio extension, surface vertical velocity induced by Stokes divergence is comparable to the Ekman velocity, and may alter the meso-scale dynamics of the front.

1. Introduction

The Stokes drift is one of the manifestations of ocean surface waves, and impacts mass and momentum transports near the surface. An accurate evaluation of the Stokes drift and the inclusion of related processes may lead to improved representation of surface physics in ocean general circulation model (OGCM) [e.g., McWilliams and Restrepo 1999]. In addition, the Stokes drift and associated vortex force have been considered to be the mechanisms responsible for the Langmuir circulation (LC) [e.g., Leibovich, 1983; McWilliams et al. 1997]. The additional turbulence kinetic energy (TKE) due to Stokes

velocity shear production is also crucial for vertical mixing in the upper ocean [e.g., Kantha and Clayson 2004].

The exact representation of wave effect on mean current field is still being debated in terms of wave-averaging techniques (Generalized Lagrangian mean, Eulerian mean), how momentum variables are separated (total momentum, quasi-Eulerian mean flow), and the underlying assumptions of wave-current coupling theories [e.g., Mellor 2003, 2008, McWilliams et al 2004, Ardhuin et al. 2008, Aiki and Greatbatch, 2012]. In the Eulerian framework in which mean flow and wave momenta are separated, the Stokes drift appears as additional divergence of mass and external forces such as the vortex force and the Stokes-Coriolis force in continuity and momentum equations [McWilliams and Restrepo 1999; McWilliams et al 2004; Weber et al. 2006; Smith 2006; Newberger and Allen 2007; Uchiyama et al 2010]. Therefore, temporal and spatial structure of the Stokes drift field can provide useful information on the significance of wave effect on mean flow field.

McWilliams and Restrepo [1999] argued that the Stokes drift could influence the ocean general circulation through modification of the Ekman pumping due to the induced mass flux. Their result was based on an empirical estimate of the Stokes drift using the wind data. Recent advances in third generation wave models make it possible to accurately

reproduce wave spectra [e.g., Ardhuin et al. 2009; 2010] and to directly estimate the Stokes drift for random directional waves in realistic wave conditions [Rascle et al. 2008; Kantha et al. 2009; Ardhuin et al. 2009; Webb and Fox-Kemper, 2011]. The present study was motivated by a desire to better understand the Stokes drift in the Pacific Ocean. We are particularly interested in estimating wave induced-mass transport near Japan in the presence of strong currents and vorticity due to the Kuroshio and Kuroshio Extension. To address these issues, we use the third generation wave model to conduct wave hindcasts and analyze the Stokes drift and wave induced-mass transport in the Pacific Ocean.

The paper is organized as follows. Section 2 describes the theoretical aspect of the Stokes drift and wave-induced mass flux. Ocean wave hindcasts are also described. In section 3, we firstly validate the model Stokes drift field against that estimated from in-situ wave spectra. Then we investigate the Stokes drift and wave induced-mass flux in the Pacific. Finally, summary and discussions are given in section 4.

2. The Stokes drift and model experiments

2.1 The Stokes drift and wave momentum

We assume deep water conditions. The vertical profile of the wave-induced

velocity is given by either the pseudo-momentum of Andrews and McIntyre [1978] or the Stokes drift velocity [Longuet-Higgins, 1953]. For wave motions that are horizontally homogeneous and irrotational in the vertical plane, analytical expressions for the pseudo-momentum and the Stokes drift velocity are the same and may be written as

$$\bar{\boldsymbol{u}}^{St}(z) = \boldsymbol{U}_S \cdot \exp(z / D_S) \qquad (1)$$

where z is the vertical axis, $\boldsymbol{U}_S$ is the Stokes drift velocity at the surface ($=\sigma \boldsymbol{k} a^2$), D_S is the stoke depth scale ($=1/2k$), $\boldsymbol{k}=k(\cos\theta, \sin\theta)$ is wavenumber vector, σ is angular frequency, k is wavenumber, θ is wave direction and a is wave amplitude. The Stokes drift velocity for random directional waves is derived by extending equation (1) for wave spectrum $F(\sigma,\theta)$ assuming a statistically stationary and horizontally homogeneous wave field [Kenyon, 1969]:

$$\bar{\boldsymbol{u}}^{St}(z) = \frac{2}{g}\iint \sigma^3 F(\sigma,\theta)\boldsymbol{k}/k \cdot \exp(2kz)\, d\sigma d\theta \qquad (2)$$

where g is gravitational acceleration, and $F(\sigma,\theta)d\sigma d\theta = 0.5a^2$.

Equation (2) is cumbersome for evaluating the Stokes drift in a realistic ocean wave field since it requires the wave spectral shape. Additionally the integrand includes an exponential function which decays according to the wavenumber k, so that vertical profiles of Stokes drift also depend on the spectral shape. The concept of "the Stokes *e*-folding

depth" [Li and Garrett, 1993; Harcourt and D'Asaro, 2008] is useful for representing the penetration depth of Stokes drift for random directional wave field, because Equation (2) can then be parameterized to the same form as equation (1) using the surface Stokes drift $\boldsymbol{U}_S$ and the Stokes *e*-folding depth D_S^*:

$$\overline{\boldsymbol{u}}^{St}(z) = \boldsymbol{U}_S \cdot \exp(z / D_S^*) \tag{3}$$

where, $\boldsymbol{U}_S = 2g^{-1}\iint \sigma^3 F(\sigma,\theta)(\cos\theta, \sin\theta) d\sigma d\theta$, D_S^* is defined as the depth where $\overline{u}^{St}(z = -D_S^*)/U_S = e^{-1}$. The surface Stokes drift $\boldsymbol{U}_S$ in equation (3) is an exact expression which is evaluated using the third moment of frequency spectrum. On the other hand, the Stokes *e*-folding depth D_S^* is not directly estimated from wave parameters; to evaluate it one needs to know the exact vertical profile of the Stokes drift for random directional wave fields which is expressed by equation (2).

It is also possible to define the wave induced-mass transport in Eulerian coordinate where mean wave momentum is distributed between the wave crests and the troughs. The total mass transport due to ocean waves $\boldsymbol{M}^w$ (or total wave momentum) is evaluated at the mean surface by applying the Taylor expansion with second order accuracy,

$$\boldsymbol{M}^w \equiv \rho \overline{\int_{\overline{\zeta}}^{\overline{\zeta}+\zeta'} (\overline{\boldsymbol{u}} + \boldsymbol{u}') dz} \approx \rho \overline{\boldsymbol{u}'\zeta'}\Big|_{z=\overline{\zeta}} \tag{4}$$

where, ρ is water density, $\overline{\zeta}$ and $\overline{\boldsymbol{u}}$ are wave-averaged components of surface elevation

and velocity vector, ζ' and $\boldsymbol{u}'$ are wave components. By substituting the first-order solution of surface wave to equation (4), we get

$$\boldsymbol{M}^{w} = 0.5\rho a^2 \sigma \mathbf{k} / k = \rho \iint \sigma \cdot F(\sigma,\theta) \cdot \mathbf{k} / k \cdot d\sigma d\theta \qquad (5)$$

In linear wave theory, the wave induced-mass transport in Eulerian coordinate (equation 5) is equal to the Stokes transport (depth integral of the Stokes drift velocity, equation 2) [e.g., Phillips 1977];

$$\boldsymbol{M}^{w} = \rho \int_{-\infty}^{\bar{\zeta}} \overline{\boldsymbol{u}}^{St}(z) dz \approx \rho \int_{D_S^*}^{\bar{\zeta}} \overline{\boldsymbol{u}}^{St}(z) dz \qquad (6)$$

Again, the *e*-folding depth D_S^* is an indication of the significant penetration depth of the Stokes drift. Three-dimentional wave-averaged equations of mean current required vertical profile of the Stokes drift [e.g., McWilliams et al, 2004; Uchiyama et al, 2010], whereas formulation based on the depth integrated equations (2D) utilize total wave momentum as the boundary condition at the mean surface [e.g., Hasselmann 1971; Garett 1976; Ardhuin et al 2004; Smith 2006]. In this study, we investigate the structure of the Stokes drift and the Stokes transport as the total wave induced-mass flux estimated using wave spectra obtained from ocean wave hindcasts.

2.2. Ocean wave hindcasts

Wave hindcast is conducted based on WAVEWATCH-III^{TM} version 3.14 [WW3; Tolman, 2009] to provide estimates of the Stokes drift and wave-induced mass flux. We used a nested model domain for grid resolution of 1 degree (nest1) and 0.25 degree (nest2). The outer nest (nest1) covers the Pacific Ocean excluding the polar regions (66°S–66°N latitude and 100°E–290°E longitude). The inner nest (nest2) is used to investigate the effect of the mean surface current on waves fields and associated modulation of wave-induced mass transport in the Northwestern Pacific (20°S–50°N latitude and 117°E–180°E longitude). Tolman and Chalikov's [1996] source terms are used, and the surface wind speed at 10 m elevation (U_{10}) is modified to account for the instability of the atmospheric boundary layer (the “effective” wind speed; Tolman, 2002). We also employ the discrete interaction approximation (DIA) method as the nonlinear transfer function *Snl* [Hasselmann et al. 1985]. The spectral space is discretized using 35 frequencies ranging from 0.041 Hz to 1.05 Hz (relative frequency of 10%, $f_{m+1} = 1.1f_m$, where m is a discrete grid counter) with 36 directions ($\Delta\theta = 10°$). We assume an f^{-5} spectral tail outside the model frequency range, as used in the default WW3 settings. For spatial propagation of the wave spectrum, we use the default third-order advection scheme.

The hindcast is performed for a five-year period from 2006 to 2010. The wave

model is driven by 6-hourly wind stress from the National Centers for Environmental Prediction/National Center for Atmospheric Research (NCEP/NCAR) reanalysis product [Kalnay et al., 1996], in which the global data set has a resolution of 192 × 94 gaussian grids. The ETOPO5 [http://www.ngdc.noaa.gov/mgg/global/etopo5.HTML] is used to define the bottom topography and coastlines. In addition, we utilized the weekly ocean current products with 0.25 degree resolution by Ambe et al [2010]. Ambe et al [2010] proposed a new scheme to estimate mean surface geostrophic velocity using satellite altimeter (Maps of Sea Level Anomaly product provided by AVISO) and drifter data (assembled by the Surface Velocity Program by AOML). Therefore, model results of nest2 include the effect of geostrophic mean flow on ocean wave field. As the boundary condition, the hourly boundary spectral data was provided from the nest1 model results.

3. Results

3.1. Validation

In general, third-generation wave models can represent the pronounced peak of wave spectra for growing sea and have successfully reproduced the f^{-4} power law in the equilibrium range using an appropriate *Snl* [e.g., Resio and Perrie, 1991; Komatsu and

Masuda, 1996; Tamura et al, 2008]. Therefore, third-generation wave models have great potential for the evaluation of wave spectra. However, the surface Stokes drift and wave induced-mass transport investigated in this study are evaluated as higher-order moment of wave spectrum (Equation (2) and (5)). These quantities can be sensitive to the parameterization of higher frequency spectral tail. We therefore firstly validate the model performance of WW3 on the surface Stokes drift and the total mass transport estimated from wave spectra at six NOAA/NDBC buoys deployed in deep waters, mainly in the northeastern Pacific (Fig. 1).

Table 1 lists the performance of the wave model against observations in terms of the surface Stokes drift. In this validation, we used observed wave spectra at NDBC buoys with higher-resolution (frequency bin size: 0.005~0.02 Hz, frequency range: from 0.02 to 0.485 Hz). Because available in-situ data for directional spectrum are limited (only lower-order Fourier coefficients of the directional spreading function are available), we neglected the directionality of the surface Stokes drift in this validation. The magnitude of the surface Stokes drift estimated by modeled wave spectrum (U_S^s: WW3spec) is,

$$U_S^s = 2g^{-1}\int_0^{\sigma_c} d\sigma \cdot \sigma^3 \int_{-\pi}^{\pi} F(\sigma,\theta) d\theta \qquad (7)$$

where, σ_c is cut-off angular frequency set to be 0.49 Hz so as to approximate the cut-off

frequency of observed wave spectra (0.485 Hz). For comparison, we also compute the surface Stokes drift using bulk wave parameters (U_S^b: WW3bulk) such as the significant wave height H_s and peak period T_p (=$2\pi/\sigma_p$),

$$U_S^b = \sigma k a^2 = g^{-1}\left(\frac{2\pi}{T_p}\right)^3\left(\frac{H_s}{2\sqrt{2}}\right)^2 = g^{-1}\pi^3 H_s{}^2 T_p{}^{-3} \quad (8)$$

This estimation is derived from equation (2) assuming a monochromatic wave condition. While the third moment of frequency spectrum can more accurately represent the Stokes drift field [Webb and Fox-Kemper, 2011], peak values of the frequency spectrum have previously been used in the literature as representative quantities to investigate the effect of wave-induced mixing [e.g., Wu and Liu, 2008; Huang et al. 2011]. In this study, we discuss the applicability of the bulk parameterization of equation (8).

Two other parameterizations of the surface Stokes drift proposed by Ardhuin et al [2009; hereinafter AMRFR09; their equation (C3)] and Li and Garrett [1993; hereinafter LG93, their equation (18)] are also evaluated. All physical quantities required for the surface Stokes drift estimation such as U_{10}, H_s, T_p, and $F(\sigma)$ are model products from NCEP/NCAR Reanalysis and WW3.

The WW3spec and AMRFR09 parameterizations performed quite well for all

statistical scores; the normalized bias (NB) is within 10% (except 51100), the root mean squared error (RMSE) is less than 5cm/s and correlation coefficient (CC) is 0.8-0.9 at all buoy locations. These results suggest that WW3spec and AMRFR09 are sufficiently robust and applicable to representing the surface Stokes drift field in the Pacific. On the other hand, WW3bulk does a poor job in representing the Stokes drift; NB is less than -60 % (significant underestimation) and CC is substantially lower than WW3spec and AMRFR09 parameterizations. Moreover, the performance of WW3bulk is significantly poorer than LG93 which only uses the surface wind speed (the surface Stokes drift is evaluated as 1.5% of U_{10}). It is worth mentioning that parameterization by AMRFR09 uses wind speed and wave bulk parameters whereas WW3bulk uses only wave parameters. Therefore, a key point is how to consider physical properties of the surface Stokes drift. As will be discussed later, the surface Stokes drift is strongly related to the temporal evolution of the spectral energy in the equilibrium range. On the other hand, wave bulk parameters such as *Hs* and T_p represent the spectral properties around the spectral peak. Therefore, parameterization based on the wind speed rather than wave parameters may provide a more accurate first-order approximation to the surface Stokes drift. Table 2 also lists the performance of WW3spec on the Stokes transport at the same locations, indicating the practical

applicability of WW3.

3.2. Stokes drift in the Pacific Ocean

Figure 1 (a) shows annual mean of the Stokes drift velocity at the surface U_S^s (equation 7) and the Stokes *e*-folding depths D_S^*, directly estimated by equation (2) in the Pacific Ocean. In the following analysis of the Stokes drift field, the cut-off frequency σ_c is set to be 1.05 Hz as full spectrum of model frequency domain. In the mid-latitudes from 35°N to 55°N, the mean Stokes drift is eastward largely corresponding to the westerlies. In low latitudes, the strong Stokes drift is oriented roughly in the westward direction, corresponding to Intertropical Convergence Zone (ITCZ) between 20°S and 25°N. The range of the mean D_S^* is small from about 1 to 2m, and its spatial characteristics can be roughly categorized into 2 domains: the north Pacific (NP; 40°N-55°N) and ITCZ (20°S-30°N). The local peak of the annual mean U_S^s appears in the NP (150-140°W, 45-55°N) and in the ITCZ (160-140°W, 10-20°N and 100-80°W, 15-5°S). The mean D_S^* is deeper than 1.5m in NP whereas it is shallower than 1.5m in ITCZ.

These features of the Stokes drift field can be explained by the properties of ocean wave spectra in the Pacific. Large mechanical wind energy is transferred to surface waves

in the mid-latitudes from 30° to 60° N [e.g., Wang and Huang, 2004], corresponding to strong surface wind fields associated with storm tracks. The variations of wave spectrum are characterized by strong downshifting of the peak frequency due to the *Snl* [Hasselmann et al. 1973]. Corresponding to the high windsea energy with lower spectral peak (less than about 0.1Hz), U_S^s and D_S^* become large in NP, because higher frequency component of wave spectrum contributes substantially to the surface Stokes drift whereas lower frequency component affects deeper part. Ocean waves generated in the mid-latitudes propagate far from storms and radiate eastward in the tropical and subtropical Pacific as swells. At lower latitudes, especially in ITCZ, trade winds blowing predominantly from the ENE and ESE constantly generate local windsea with background swells, sporadically coming from higher latitudes. Therefore, the wave spectra are characterized by bi-modal shape; stationary higher frequency peaks (around 0.12Hz) with slowly upshifting spectral peaks at low frequency (less than about 0.1Hz) [Tamura et al, 2010]. Because spectral energy due to short waves is now dominant, U_S^s become large but it drops rapidly with depth. Thus D_S^* become small in the ITCZ regions.

The spatial characteristics of the Stokes drift field thus depend on the spectral shape. Therefore, one expects the Stokes drift field estimated using bulk parameters

(surface Stokes drift U_S^b evaluated by equation (8) with *e*-folding depth as $D_S^b = 1/2k_p$) to differ significantly from that shown in Fig.1a. Figure 1b indicates that the surface Stokes drift is significantly lower compared with that of Figure 1a; significant negative biases were also found in comparison with observations (Table 1). Figure 1b also shows that the corresponding Stokes *e*-folding depth D_S^b computed using the bulk formulation is grossly overestimated over the entire region of the Pacific Ocean, by as much as 5-20 times larger. Moreover, the spatial distribution of D_S^b is zonal (Fig.1b), whereas D_S^* shows a predominantly meridional variation (Fig.1a). The discrepancy is explained by the predominance of swell propagation from higher latitude in case of bulk parameterization, which only has contribution from the lower-frequency component of the wave spectrum with no contributions from the higher frequencies.

Figures 2 shows the joint probability distribution function of (a) the surface Stokes drift: U_S^s verses U_S^b, and (b) Stokes *e*-folding depth: D_S^* verses D_S^b. These demonstrate that significant discrepancies exist when the bulk parameters are used to estimate the Stokes drift field. The surface Stokes drift U_S^b computed using bulk parameters tend to be underestimated as compared with U_S^s computed directly from the wave spectrum. The Stokes *e*-folding depth D_S^b is grossly overestimated, and has little correlation with D_S^*.

Since parameterization of the surface Stokes drift by equation (8) with *e*-folding depth of $D_S^b = 1/2k_p$ is derived from equation (2) assuming a monochromatic wave field, the two equations become identical for a sufficiently narrow spectrum. However, the spectrum of ocean surface wave is broad so as to invalidate the assumption. Therefore, appropriate treatments of the wave spectrum are required for evaluating the surface Stokes drift and *e*-folding depth.

To gain insight into forcing parameters of large eddy simulation (LES) and their most probable values in numerical experiments of LC, we evaluated the turbulent Langmuir number La_t $(=(u_\tau / U_S)^{0.5}$, where u_τ is the friction velocity for water side, and the Stokes *e*-folding depth D_S^*. In addition, the relevance of La_t and D_S^* will provide the physical understanding of the Stokes drift for the realistic wave condition. Figure 3a shows the joint-probability distribution function of La_t and D_S^* in the North Pacific from 2006 to 2010. The most probable values of La_t and D_S^* are approximately 0.3 to 0.35 and 0.7 to 1.4m, respectively. The La_t value is consistent with that found in previous works [e.g., Figure 2 in Harcourt and D'Asaro 2008], whereas D_S^* is 2~10 times smaller than those used in the literature [e.g. D_S^* ≈ 10 m by Polton et al 2005, and ≈ 6 m by Min and Noh 2004]. Fig. 3a also shows that La_t and D_S^* tend to be negatively correlated. This is because

La_t represents the ratio of friction velocity and the surface Stokes drift, and U_S increases rapidly during the wave growth because wind energy is initially funneled to wave energy in higher frequency region (equilibrium range). Therefore, La_t decreases during the evolution of the wave spectrum. On the other hand, the Stokes *e*-folding depth D_S^* represents the depth where the subsurface Stokes drift velocity has decayed to e^{-1} of its surface value. While U_S tends to saturate, the subsurface Stokes drift can increase during the wave growth, since higher-frequency components of wave spectrum are embedded within an equilibrium range and lower-frequency components increase due to the downshifting of spectral peak. Therefore, the Stokes depth tends to increase during the spectral evolution. Mean inverse wave age for windsea (Figure 3b) actually indicates that it become large when La_t is large (0.4-0.5) and D_S^* is small (0.3-0.7m) which correspond to young wind sea.

3.3. The wave-induced mass flux in the northwestern Pacific

The depth integrated equations of wave-current coupling in Eulerian coordinate suggest that the divergence and convergence of wave induced-mass flux act as sources and sinks of mean flow field at the mean surface [Hasselmann 1971; Garrett 1976; Ardhuin et al.

2004; Smith 2006],

$$\partial_t \overline{\zeta} + \rho^{-1} \nabla \cdot \boldsymbol{M}^m = -\rho^{-1} \nabla \cdot \boldsymbol{M}^w \qquad (9)$$

where ∂_t is time derivative, $\boldsymbol{M}^m$ is depth integrated momentum mean flow. In this subsection, we investigate the impact of total wave momentum $\boldsymbol{M}^w$ (or Stokes transport) in the northwestern Pacific using nest2 model results.

Figure 4 show (a) monthly mean significant wave height and wave induced-mass transport $\boldsymbol{M}^w$ and (b) the negative of its divergence $-\rho^{-1} \nabla \cdot \boldsymbol{M}^w$ (i.e. right hand side of equation 9) with mean geostrophic current in February 2007. The spatial distributions of mean wave height and mass transport roughly correspond to the synoptic scale (~1000km). Mean wave height is large in mid-latitudes (30-45°N) due to the westerlies and storm tracks. Associated with the wave field, wave induced-mass flux is south-eastward in the mid-latitudes and south and southwestward in low latitudes (20-25°N) in the northwestern Pacific.

On the other hand, the divergence of wave induced-mass flux is significantly modified by the effect of local fetch, coast, and ocean current (Figure 4b) and its spatial scale correspond to meso-scale features (100~500km). The $-\rho^{-1} \nabla \cdot \boldsymbol{M}^w$ is largely negative (sea level down), especially off the Tohoku coast (37-43°N, 142-143°E) and

Kuroshio extension region (142-170°E, 30-40°N). On the contrary, $-\rho^{-1}\nabla\cdot\boldsymbol{M}^{w}$ is positive (sea level rise) along the western and northern coast of Japan and in some parts of the Kuroshio extension region.

These spatial patterns of enhanced mass divergence and convergence regions can be explained by seasonal wind and associated wave fields. Again, ocean wave develops largely due to the westerlies and storm tracks in the northwestern Pacific in boreal winter. Especially, due to the high-wind speed conditions off the Tohoku [e.g., Sampe and Xie, 2007], ocean waves develop abruptly from the eastern coast (Figure 4a) and divergence of wave induced-mass transport contributes to the set-down of mean sea surface in this region. On the other hand, western coast of Japan is where ocean waves developed in Japan Sea and significant amount of wave energy is dissipated along the coast in boreal winter. Convergence of wave mass transport (setup of mean sea surface) is induced along the western coast in boreal winter. Divergences and convergences also appear in the Kuroshio extension region where mean wave energy is increased in the countercurrent region and decreased in the along-current region due to wave refraction. These features are mostly confined to eddies and meandering Kuroshio where the corresponding wave-induced divergences and convergences produce vertical velocities of O(5-10cm/day). Although

these are weaker than values of O(10-100 m/day) often found in strong frontal zones [e.g. Chang and Oey, 2011], they are comparable to the annual and seasonal mean Ekman pumping/suction in the open ocean over the Gulf Stream and the Kuroshio [Gill, 1982; Risien and Chelton 2008]. Wave-induced divergences and convergences can therefore have important consequences to the upper-ocean dynamics in which wind, ocean currents and surface gravity waves are coupled. Figure 5 shows ocean geostrophic currents on color maps of (a) wind speed and (b) wind stress curl computed from the Cross-Calibrated Multi-Platform (CCMP) product [Atlas et al. 2011]. Westerly wind blowing across the Japan Sea is channeled through the Tsugaru Strait (because of higher elevations on either sides of the Strait, Shimada et al. 2010), and becomes maximum some 1000 km downstream as it expanded over the ocean to the northern wall of the Kuroshio.

Along the Kuroshio, strong air-sea coupling is seen with high (low) wind speeds over warm (cold) waters [Risien and Chelton, 2008] (Fig. 5a), giving rise to meso-scale wind stress curls anchored to the current meanders (Fig. 5b). Contours of $|R|$ ($R = \nabla \cdot \boldsymbol{M}^w / \nabla \times \boldsymbol{\tau}_{wind} / f$) display streak-like structures aligned with the axes of maximum wind speeds and/or strong currents where $\rho^{-1}\nabla \cdot \boldsymbol{M}^w$ tends to be strong and $\rho^{-1}\nabla \times \boldsymbol{\tau}_{wind} / f$ weak; i.e. waves effects are largest where Ekman pumping is weakest. The

winter's westerly winds produce predominantly divergent Stokes transports along the Kuroshio meander (Fig. 4b), and the resulting set-down in free-surface elevation enhances (reduces) Ekman downwelling (upwelling), as shown in Fig. 6 where the signed "*R*" is overlaid on color maps of wind speed and Ekman vertical velocity along a portion of the Kuroshio extension. Positive (negative) "*R*" indicates regions where the Ekman vertical velocities, either upwelling or downwelling, are enhanced (reduced) by the Stokes divergence. Because of air-sea coupling, there is, in general, Ekman upwelling along a southward meander, and Fig. 6 shows that the upwelling is weakened by the Stokes divergence. Along a northward meander, the west-northwesterly wind tends to blow across the front and would give little or weak divergence. However, the asymmetric meander produces also an asymmetric arrangement of winds along the meander that favors Ekman downwelling, albeit weak, along the northward portion of the meander, e.g. Fig. 6b near 161E & 167E.

In boreal summer, mean wave height and wave induced-mass transport (Figure 4c) are lower than those of boreal winter and the corresponding divergences and convergences (Figure 4d) become small in the northwestern Pacific. But significant mass convergence appears along the southeastern coast of China. These convergences are largely caused by

the summer monsoon winds. Five-year average of the wave induced-mass flux (Figure 4f) shows that mass divergence regions extend approximately 200-500km offshore along the eastern coast exposed to the Pacific, Japan Sea, and East China Sea. This is induced by the effect of local fetch and related wave development. On the other hand, significant mass divergence and convergence regions disappear in the Kuroshio extension region in five-year average, because these divergences and convergences are induced by eddies and Kuroshio meanders, and they tend to cancel in the average.

4. Summery and Discussions

In this study, we investigated the Stokes drift and wave induced-mass flux in the north Pacific using the third-generation wave model (WW3) driven by surface wind and geostrophic current. The wave model performed well in representing the Stokes drift field and total wave momentum when compared with NDBC buoy data. Five-year hindcasts of ocean waves and estimated Stokes drift in the north Pacific suggest that most probable values of the surface Stokes drift range from about 1 to 18cm/s and the Stokes *e*-folding depth is 0.5 to 3m. On the other hand, the Stokes drift fields estimated by bulk wave parameters are very different from those estimated directly from wave spectra. The bulk

formulation significantly underestimates the surface Stokes drift and overestimates the *e*-folding depths. The choice for the two forcing parameters La_t and D_S^* in LES experiments is often quite arbitrary. This study demonstrates that La_t and D_S^* tend to be negatively correlated and this feature can be explained by considering the spectral evolution of ocean surface waves [Tamura et al 2010]. The spatial distributions of mean wave height and mass transport approximately follow the synoptic scale associated with atmospheric forcing.

The divergence of wave induced-mass flux is significantly modified by local fetch, the coast and ocean currents. Our results show significant convergences along the Japan coast and the southeastern coast of China in the annual mean field. The model's grid sizes are presently too coarse to resolve detailed profile of mass transport associated with ocean waves in these near-shore regions [Newberger and Allen, 2007]; further research is clearly needed to understand the processes. On the other hand, as pointed out above in the open ocean there are significant mass divergences and convergences caused by the combined effects of the seasonal winds, local fetch and ocean currents, and the estimated vertical velocity is comparable to Ekman pumping/suction. McWilliams and Restrepo [1999] indicated that total wave momentum at the mean surface is canceled by Stokes transport in

the vertically integrated vorticity equation and therefore, the wave induced vorticity inputs which are related to the Stokes-Coriolis force become zero. However, wave effects on the mean vorticity field still remain through the $\partial_t \overline{\zeta}$ term in the continuity equation which is modulated by divergence and convergence of the wave induced-mass fluxes $\rho^{-1}\nabla \cdot \boldsymbol{M}^w$.

Mean vertical velocities estimated from wave induced-mass divergence are comparable with Ekman pumping/suction in the Kuroshio extension region in boreal winter. In addition to being crucial in small-scale mixing processes (e.g. Langmuir cells), the Stokes transport may therefore also play an important role in meso and larger scale upper-ocean dynamics through its contributions to the ocean's surface convergences and divergences. Spall [2007] suggests that, because of air-sea coupling, the growth rate of baroclinic disturbance along an SST front is enhanced (reduced) by wind blowing from the warm (cold) side of the front. Our analyses (Figs.5 and 6) suggest that the presence of surface gravity waves may alter the growth rate because the coupling of the wind, ocean currents and waves always give rise to a Stokes transport divergence $\rho^{-1}\nabla \cdot \boldsymbol{M}^w$ that is *opposite* to the Ekman pumping or suction, so that waves tend to be stabilizing (destabilizing) for wind blowing from the warm (cold) side of the front. On the other hand, other effects of waves on the large-scale circulation such as the Stokes-Coriolis force

[Hasselmann 1970], or indeed the possibility of a wave-driven wind regime (especially in the tropics, Hanley et al. 2010) which then feeds back into the ocean's circulation, may also need to be considered for a more complete understanding. These are issues that we plan to explore in future work.

The findings give insights into the physical features of the Stokes drift and useful information for practical applications of wave-current coupled modeling. For the application of wave-current coupling processes to OGCM, it is clear that high vertical resolution is required to accurately represent the Stokes drift field. As described above, the Stokes *e*-folding depth ranges within a few meters, which require vertical grid sizes of order of 10 cm near the surface. Vertical profile of the Stokes drift and associated 3D wave induced-momentum fluxes are necessary to accurately represent nearshore processes [e.g., Uchiyama et al. 2010]. However, for coupling waves in submeso-meso and larger-scale processes, the thinness of the Stokes *e*-folding depth suggests that it may be reasonable to treat wave effects as surface boundary conditions, as assumed above when discussing the Kuroshio meander.

Finally, Huang et al. [2011] discussed the importance of additional TKE due to the Stokes production [Skyllingstad and Denbo; 1985; Kantha et al 2009] and concluded that

subsurface thermal structures are improved significantly by including the Stokes production. The present study indicates that the Stokes drift is mainly confined near the surface and the *e*-folding depth is of the order of the significant wave height. The impact of additional TKE should therefore be also confined within a few meters from the surface, and missing physical processes may be required to explain the deepening of the mixed layer due to ocean waves. One plausible explanation is indicated in LES in which down-welling jets associated with LC penetrate to depths in excess of the Stokes depth scale [e.g., Polton and Belcher 2007]. However, further fundamental studies are required to clarify this problem.

Acknowledgements

The authors would like to thank two anonymous reviewers for their constructive comments, which were very helpful in improving the manuscript. The geostrophic currents data were provided by Daisuke Ambe at Fisheries Research Agency. HT also wish to acknowledge helpful discussions with Takuji Waseda (University of Tokyo) and Hidenori Aiki (JAMSTEC). This work is part of the Japan Coastal Ocean Predictability Experiment (JCOPE) supported by the Japan Agency for Marine-Earth Science and Technology (JAMSTEC). HT was supported by the Japan Society for the Promotion of Science.

References

Aiki, H., and R. J. Greatbatch (2012), Thickness weighted mean theory for the effect of surface gravity waves on mean flows in the upper ocean, *J. Phys. Oceanogr.*, 42, 725–747.

Ambe D., K. Komatsu, A. Okuno, M. Shimizu, and A. Takasuka (2010): Survival Response during Early Larval Stage of Japanese Sardine to Physical Oceanic Conditions Leading to Their Recruitment, Proceedings of Techno-Ocean 2010 CD-ROM, 2010

Andrews, D.G. and M.E. McIntyre (1978), An exact theory of nonlinear waves on a Lagrangian mean flow, J. Fluid Mech, 89, 609–646.

Ardhuin, F., B. Chapron, and T. Elfouhaily (2004), Waves and the air-sea momentum budget, implications for ocean circulation modelling, *J. Phys. Oceanogr*., 34, 1741–1755.

Ardhuin, F., N. Rascle, and K.A. Belibassakis (2008), Explicit wave-averaged primitive equations using a generalized Lagrangian mean, Ocaean Modell., 20, 35-60.

Ardhuin, F., L. Marié, N. Rascle, P. Forget, and A. Roland (2009), Observation and Estimation of Lagrangian, Stokes, and Eulerian Currents Induced by Wind and

Waves at the Sea Surface, *J. Phys. Oceanogr.*, 39, 2820-2838, doi: 10.1175/2009JPO4169.1

Ardhuin, F., et al. (2010), Semi-empirical dissipation source function for wind-wave models: Part 1. Definition, calibration and validation at global scales, *J. Phys. Oceanogr*., 40, 1917–1941, doi: http://dx.doi.org/10.1175/2010JPO4324.1

Atlas, R., R. N. Hoffman, J. Ardizzone, S. M. Leidner, J. C. Jusem, D. K. Smith, and D. Gombos (2011), A cross-calibrated, multiplatform ocean surface wind velocity product for meteorological and oceanographic applications. Bull. Amer. Meteor. Soc., 92, 157-174. doi: 10.1175/2010BAMS2946.1

Chang, Y.-L. and L.-Y. Oey (2011), Frontal circulation induced by up-front and coastal downwelling winds. *Ocean Dynamics*, DOI 10.1007/s10236-011-0435-2.

Garrett, C. (1976), Generation of Langmuir circulations by surface waves -a feedback mechanism, *J. Mar. Res*., 34, 117–130.

Gill, A. E. (1982), Atmosphere–Ocean Dynamics, Int. Geophys. Ser., vol. 30, Academic, San Diego, Calif.

Hanley, K. E., Belcher, S. E. and Sullivan, P. P. (2010), A global climatology of wind-wave interaction. *J. Phys. Oceanogr.*, 40, 1263-1282.

Harcourt, R. R., and E. A. D'Asaro (2008), Large-Eddy Simulation of Langmuir Turbulence in Pure Wind Seas, *J. Phys. Oceanogr*., 38, 1542–1562, doi: 10.1175/2007JPO3842.1

Hasselmann, K. (1970), Wave-driven inertial oscillations. *Geophys.Fluid Dyn.,* 1**,** 463–502.

Hasselmann, K. (1971), On the mass and momentum transfer between short gravity waves and larger-scale motions, *J. Fluid Mech.*, 50, 189–205.

Hasselmann, K., T.P. Barnett, E. Bouws, H. Carlson, D.E. Cartwright, K. Enke, J.A. Ewing, H. Gienapp, D.E. Hasselmann, P. Kruseman, A. Meerburg, P. Müller, D.J. Olbers, K. Richter, W. Sell, and H. Walden (1973), Measurements of wind wave growth and swell decay during the Joint North Sea Wave Project (JONSWAP), Dt. Hydrogr. Z., A8 (12), 95 pp.

Hasselmann, S., K. Hasselmann, J. H. Allender, and T. P. Barnett (1985), Computations and parameterizations of the nonlinear energy transfer in a gravity-wave spectrum. Part II: Parameterizations of the nonlinear energy transfer for application in wave models, *J. Phys. Oceanogr*., 15, 1378–1391.

Huang, C. J., F. Qiao, Z. Song, and T. Ezer (2011), Improving simulations of the upper ocean by inclusion of surface waves in Mellor-Yamada turbulence scheme, *J.*

Geophys. Res., 116, C01007, doi:10.1029/2010JC006320.

Kalnay, E., et al. (1996), The NCEP/NCAR 40-year reanalysis project, *Bull. Amer. Meteor. Soc*., 77, 437–471.

Kantha, L. H., and C. A. Clayson (2004), On the effect of surface gravity waves on mixing in the oceanic mixed layer, *Ocean Modell*., 6, 101–124.

Kantha, L. H., P. Wittmann, M. Sclavo, and S. Carniel (2009), A preliminary estimate of the Stokes dissipation of wave energy in the global ocean , *Geophys. Res. Lett*. , 36 , L02605, doi:10.1029/2008GL036193.

Kenyon, K. E. (1969), Stokes drift for random gravity waves. *J. Geophys. Res*., 74, 6991–6994.

Komatsu, K., and A. Masuda (1996), A new scheme of nonlinear energy transfer among wind waves: RIAM method, Algorithm and performance, *J. Oceanogr.*, 52, 509–537.

Leibovich, S. (1983), The form and dynamics of Langmuir circulations, *Annu. Rev. Fluid Mech*., 15, 391–427.

Li, M., and C. Garrett (1993), Cell merging and the jet/downwelling ratio in Langmuir circulation, *J. Mar. Res*., 51, 737–769.

Longuet-Higgins, M.S. (1953), Mass transport in water waves, *Philos. Trans. Roy. Soc. London* A 245, 535–581.

McWilliams, J. C., P. P. Sullivan, and C.-H. Moeng (1997), Langmuir turbulence in the ocean, *J. Fluid Mech.*, 334, 1–30.

McWilliams, J. C., J. M. Restrepo (1999), The Wave-Driven Ocean Circulation, *J. Phys. Oceanogr.*, 29, 2523-2540

McWilliams, J.C., J. M. Restrepo, and E.M. Lane, (2004), An asymptotic theory for the interaction of waves and currents in coastal waters. *J. Fluid Mech*., 511, 135–178.

Mellor, G. L. (2003), The three-dimensional current and surface wave equations. *J. Phys. Oceanogr.*, 33, 1978–1989

Mellor, G. L. (2008), The depth-dependent current and wave interaction equations: A revision. *J. Phys. Oceanogr.*, 38, 2587–2596.

Min, H. S., and Y. Noh (2004), Influence of the surface heating on Langmuir circulation. *J. Phys. Oceanogr*., 34, 2630–2641.

Newberger, P.A., and J. S. Allen (2007), Forcing a three-dimensional, hydrostatic primitive-equation model for application in the surf zone, part 1: Formulation. *J. Geophys. Res.*, 112, C08018. doi:10.1029/2006JC003472.

Phillips, O.M. (1977), The Dynamics of the Upper Ocean, Cambridge University Press, London, 336.

Polton, J. A., D. M. Lewis, and S. E. Belcher (2005), The role of waveinduced Coriolis-Stokes forcing on the wind-driven mixed layer, *J. Phys. Oceanogr.*, 35, 444–457.

Polton, J. A., and S. E. Belcher (2007), Langmuir turbulence and deeply penetrating jets in an unstratified mixed layer, *J. Geophys. Res.*, 112, C09020, doi:10.1029/ 2007JC004205.

Rascle, N., F. Ardhuin, P. Queffeulou, and D. Croizé-Fillon (2008), A global wave parameter database for geophysical applications. Part 1: Wave-current -turbulence interaction parameters for the open ocean based on traditional parameterizations, *Ocean Modell*, 25, 154-171.

Resio, D. T., and W. Perrie (1991), A numerical study of nonlinear energy fluxes due to wave-wave interactions. Part 1: Methodology and basic results, *J. Fluid Mech*., 223, 609–629.

Risien, C.M., and D.B. Chelton (2008), A Global Climatology of Surface Wind and Wind Stress Fields from Eight Years of QuikSCAT Scatterometer Data. *J. Phys. Oceanogr*.,

38, 2379-2413

Sampe, T., and S.-P. Xie (2007), Mapping high sea winds from space: A global climatology., *Bull. Amer. Meteor. Soc*., 88, 1965-1978

Shimada, T., M. Sawada, W. Sha, and H.Kawamura (2010), Low-level easterly winds blowing through the Tsugaru Strait, Japan. Part I: Case study and statistical characteristics based on observations, *Monthly Weather Review*, 138, 3806-3821

Skyllingstad, E. D., and D. W. Denbo (1995), An ocean large-eddy simulation of Langmuir circulations and convection in the surface mixed layer. *J. Geophys. Res*., 100, 8501–8522.

Smith, J. (2006), Wave-current interactions in finite depth. *J. Phys. Oceanogr*., 36, 1403–1419.

Spall, M.A. (2007). Effect of sea surface temperature-wind stress coupling on baroclinic instability in the ocean. *J. Phys. Oceanogr*., 37, 1092-1097.

Tamura, H., T. Waseda, and Y. Miyazawa (2010), Impact of nonlinear energy transfer on the wave field in Pacific hindcast experiments, *J. Geophys. Res*., 115, C12036, doi:10.1029/2009JC006014.

Tamura, H., T. Waseda, Y. Miyazawa, and K. Komatsu (2008), Currentinduced modulation

of the ocean wave spectrum and the role of nonlinear energy transfer, *J. Phys. Oceanogr.*, 38, 2662–2684.

Tolman, H. L. (2002), User manual and system documentation of WAVEWATCH-III version 2.22. Tech. Note, 222, NOAA/NWS/NCEP/MMAB, 133 pp.

Tolman, H.L. (2009), User Manual and System Documentation of WAVEWATCH III^{TM} Version 3.14.

Tolman, H. L., and D. V. Chalikov (1996), Source terms in a third-generation wind wave model, *J. Phys. Oceanogr*., 26, 2497–2518.

Uchiyama, Y., J.C. McWilliams and A. F. Shchepetkin (2010), Wave-current interaction in an oceanic circulation model with a vortex force formalism: Application to the surf zone, *Ocean Modell*., 34, 16-35.

Wang, W., and R. X. Huang (2004), Wind energy input to the surface waves, *J. Phys. Oceanogr*., 34, 1276–1280.

Webb A., and B. Fox-Kemper (2011), Wave spectral moments and Stokes drift estimation. *Ocean Modell*., 40, 273-288.

Weber, J. E. H., G. Brostrom, and O. Saetra (2006), Eulerian versus Lagrangian approaches to the wave-induced transport in the upper ocean, *J. Phys. Oceanogr.*, 36, 2106–2118.

Wu, K. and B. Liu (2008), Stokes drift-induced and direct wind energy inputs into the Ekman layer within the Antarctic Circumpolar Current, *J. Geophys. Res.*, 113, C10002, doi:10.1029/2007JC004579.

Figure captions

Table 1

Performance of modeled surface Stokes drift (*M*) against estimated surface Stokes drift based on observed frequency spectra (*O*). 4 parameterizations (WW3spec (this study), WW3bulk, AMRFR09, and LG93) are evaluated at 6 NDBC buoy locations (46002, 46006, 46066, 51001, 51003, and 51100). *NB* is normalized bias (%) defined as $NB = \frac{1}{N}\sum_{i=1}^{N}(M_i - O_i)/O_{RMS}$, *RMSE* is root mean squared error $RMSE = \left[\frac{1}{N}\sum_{i=1}^{N}(M_i - O_i)\right]^{0.5}$, *CC* is correlation coefficient of *M* with *O*, and *SI* is Scatter Index (%) $SI = \frac{1}{O_{RMS}}\left[\frac{1}{N-1}\sum_{i=1}^{N}(M_i - \overline{M} - (O_i - \overline{O}))^2\right]^{0.5}$, where *N* is number of data (acquired from 2006 to 2010), $\overline{M}, \overline{O}$ are average of model and observation, and $O_{RMS} = \left[\frac{1}{N}\sum_{i=1}^{N}(O_i)\right]^{0.5}$.

Table 2

Same as Table 1, but for performance of wave model (WW3spec) against estimated wave

induced-mass transport based on measured frequency spectra.

Figure 1

Annual mean of the surface Stokes drift velocity (arrows with white speed contours, cm/s) and Stokes *e*-folding depths (color, m) in the Pacific Ocean (shown north of 30^{o}S). (a) The surface Stokes drift is estimated by equation (7) (U_S^s; WW3spec) and the Stokes *e*-folding depth D_S^* is directly estimated from equation (2) as following; Equation (2) is firstly discretized with 0.1 m resolution in depth to evaluate the vertical profile of the Stokes drift $\overline{u}^{St}(z)$. Then D_S^* is linearly interpolated from the nearest depths z_1 and z_2 which satisfy $\overline{u}^{St}(z_2)/U_S < e^{-1} < \overline{u}^{St}(z_1)/U_S$. (b) The surface Stokes drift is estimated by equation (8) (U_S^b; WW3bulk) and the Stokes *e*-folding depth D_S^b is simply estimated by $D_S^b = 1/2k_p$.

Figure 2

The joint-probability distribution function of (a) surface Stokes drift: U_S verses U_S^b, and (b) Stokes *e*-folding depth: D_S^* verses D_S^b. Hindcast results are collocated at 12 hourly and 5° intervals from 150°E to 130°W in longitude and 0-50°N in latitude (north Pacific).

Figure 3

(a) The joint-probability distribution function of LES forcing parameters: La_t and D_S^* and (b) mean inverse wave age for windsea component. Turbulent Langmuir number La_t is evaluated as $(u_\tau/U_S)^{0.5}$. Data source is same as Figure 2.

Figure 4

(a) Monthly mean significant wave height (color; meter) and wave induced-mass transport (vector; m^2s^{-1}), and (b) divergence of mass transport $\rho^{-1}\nabla\cdot\boldsymbol{M}^w$ and geostrophic velocity vectors (larger than 20cm/s) for February 2007; the latter is from Ambe et al [2010] in February 2007. (c) and (d); same as Figure 4 (a) and (b), respectively, but for August 2007. (e) and (f); same as Figure 4 (a) and (b), but for five year-average (2006-2010).

Figure 5

(a) Satellite-derived mean geostrophic velocity (vectors; larger than 35cm/s) in Feb/2007 superimposed on the corresponding mean wind speeds (color). Contours are absolute values of the ratio (25% (white), 50% (gray) & 100% (black)) of wave-induced vertical velocity at the surface to the Ekman pumping/suction calculated from the wind stress curl. (b) Same

but colors are Ekman vertical velocity $\nabla \times \boldsymbol{\tau}^{o}/(f\rho)$.

Figure 6

(a) Satellite-derived mean geostrophic velocity (vectors) in Feb/2007 superimposed on the corresponding mean wind speeds (color; m/s) in the Kuroshio extension. Cross-hatched regions are where values of the ratio (%) of wave-induced vertical velocity at the surface to the Ekman pumping/suction calculated from the wind stress curl are more (less) than +25% (-25%); dark hatches are positive and grey hatches are negative. (B) Same but colors are Ekman vertical velocity $\nabla \times \boldsymbol{\tau}^{o}/(f\rho)$ (cm/day).

Location		NB (%)	RMSE (cm/s)	C.C.	SI (%)
46002	ww3spec	-2.06	2.84	0.91	22.3
N: 25327	ww3bulk	-64.42	9.70	0.71	41.2
	AMRFR09	-2.80	3.44	0.86	27.0
	LG93	6.83	4.89	0.70	37.9
46006	ww3spec	6.45	2.71	0.91	22.0
N: 11522	ww3bulk	-63.47	8.92	0.74	40.8
	AMRFR09	3.78	3.19	0.87	26.7
	LG93	12.70	4.69	0.72	37.6
46066	ww3spec	-2.42	3.80	0.89	24.7
N: 31447	ww3bulk	-59.20	11.02	0.75	40.6
	AMRFR09	-2.61	4.56	0.83	29.6
	LG93	2.87	5.97	0.69	38.8
51001	ww3spec	9.37	2.04	0.88	21.1
N: 32832	ww3bulk	-68.13	6.80	0.62	35.9
	AMRFR09	-1.24	2.23	0.82	25.2
	LG93	23.04	3.37	0.74	30.5
51003	ww3spec	-6.18	2.23	0.78	25.8
N: 36684	ww3bulk	-73.29	6.88	0.51	36.5
	AMRFR09	-7.51	2.55	0.70	29.4
	LG93	19.19	2.95	0.70	29.4
51100	ww3spec	21.81	2.19	0.89	21.2
N: 14753	ww3bulk	-67.54	5.46	0.59	34.4
	AMRFR09	15.92	2.19	0.79	25.8
	LG93	46.09	4.04	0.74	31.8

Location	NB (%)	RMSE (m2/s)	C.C.	SI (%)
46002	-1.50	0.153	0.92	26.7
46006	0.08	0.153	0.92	25.8
46066	-0.06	0.217	0.90	29.8
51001	1.50	0.095	0.87	26.6
51003	-4.89	0.084	0.80	27.7
51100	5.35	0.070	0.90	21.7

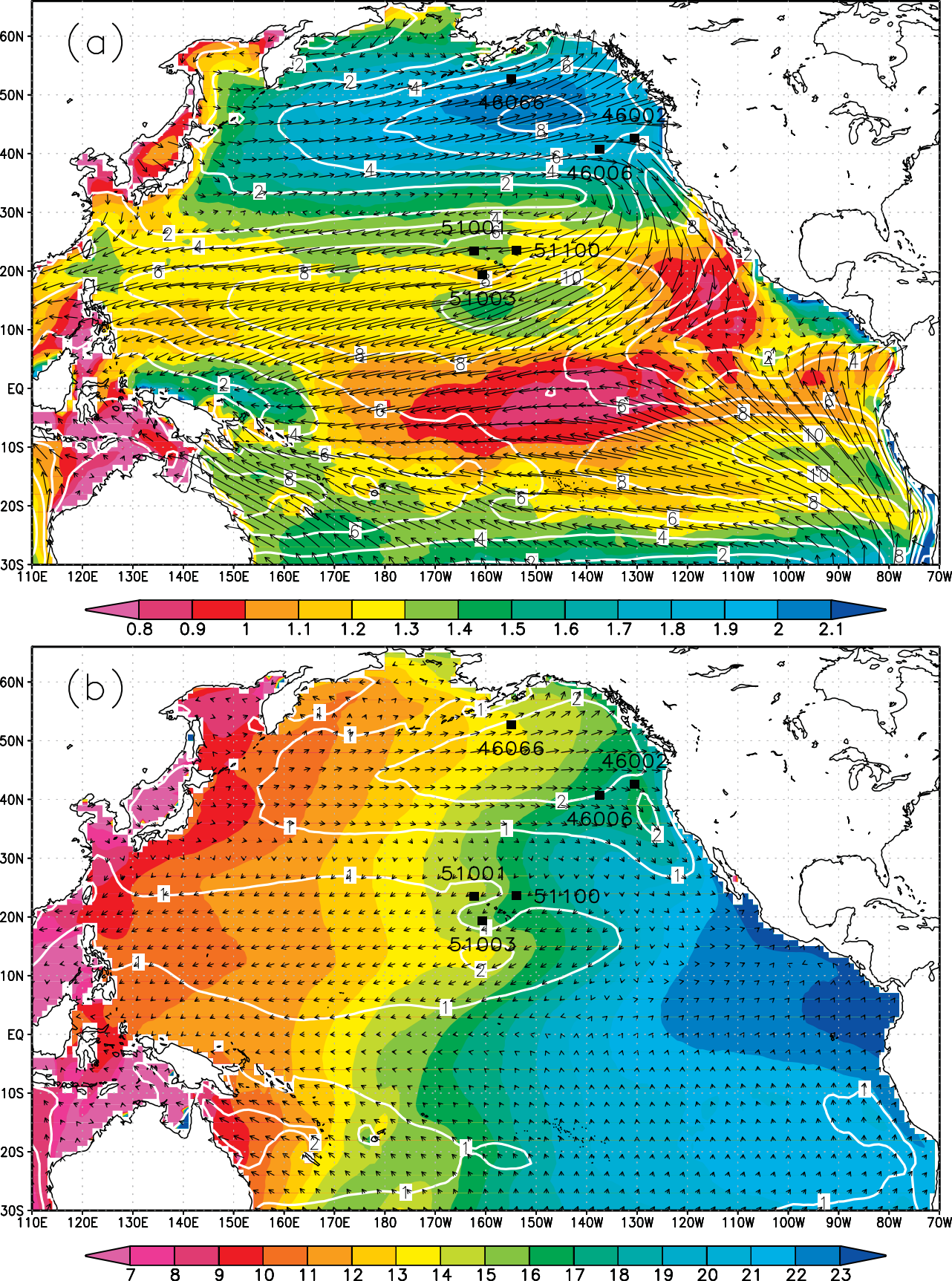
(a)
46066
46002
46006
51001
51100
51003
60N
50N
40N
30N
20N
10N
EQ
10S
20S
30S
110E
120E
130E
140E
150E
160E
170E
180
170W
160W
150W
140W
130W
120W
110W
100W
90W
80W
70W
0.8
0.9
1
1.1
1.2
1.3
1.4
1.5
1.6
1.7
1.8
1.9
2
2.1
(b)
46066
46002
46006
51001
51100
51003
7
8
9
10
11
12
13
14
15
16
17
18
19
20
21
22
23

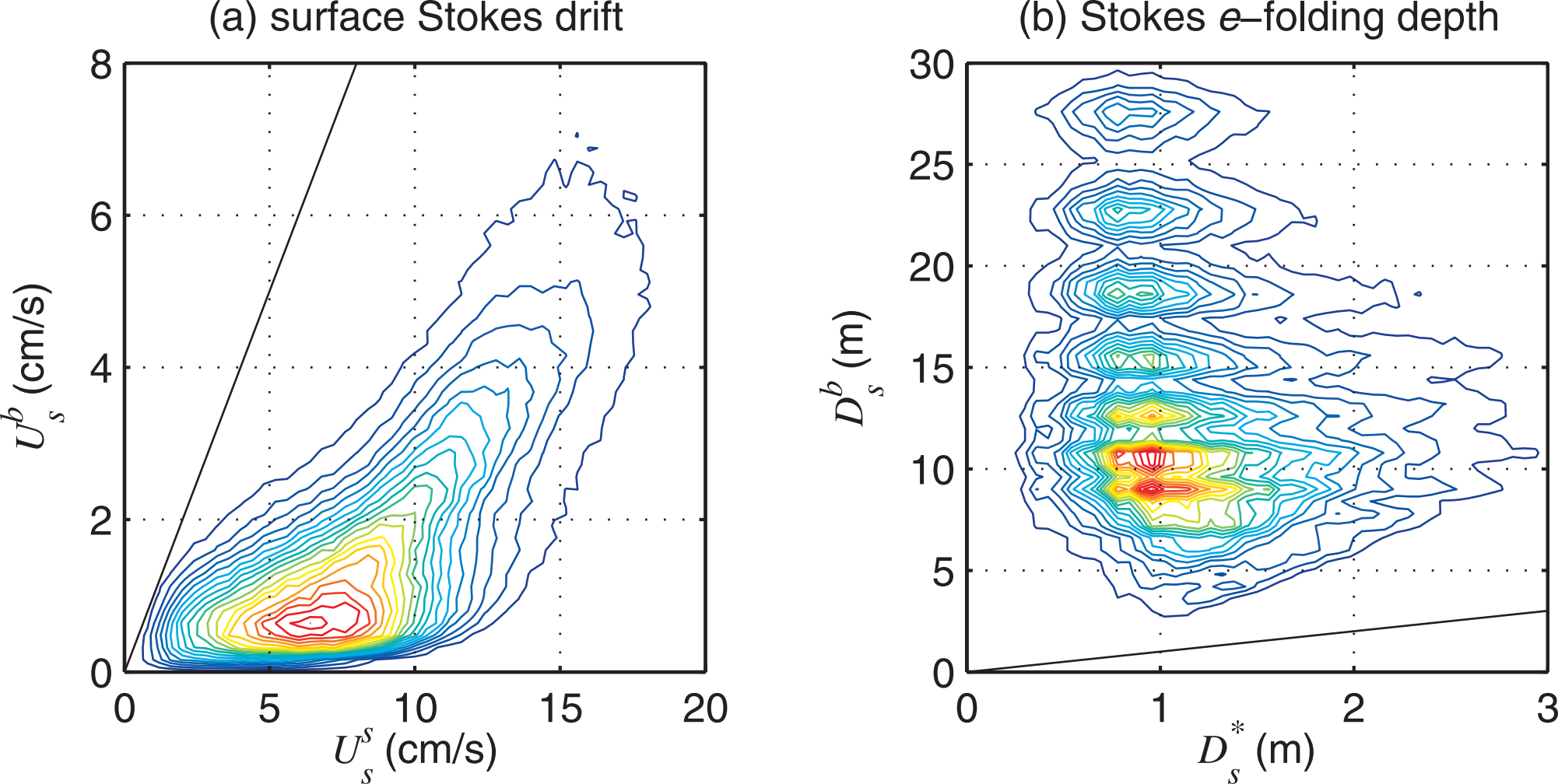
(a) surface Stokes drift
(b) Stokes e–folding depth
U_s^b (cm/s)
U_s^s (cm/s)
D_s^b (m)
D_s^* (m)
0
2
4
6
8
5
10
15
20
25
30
1
3

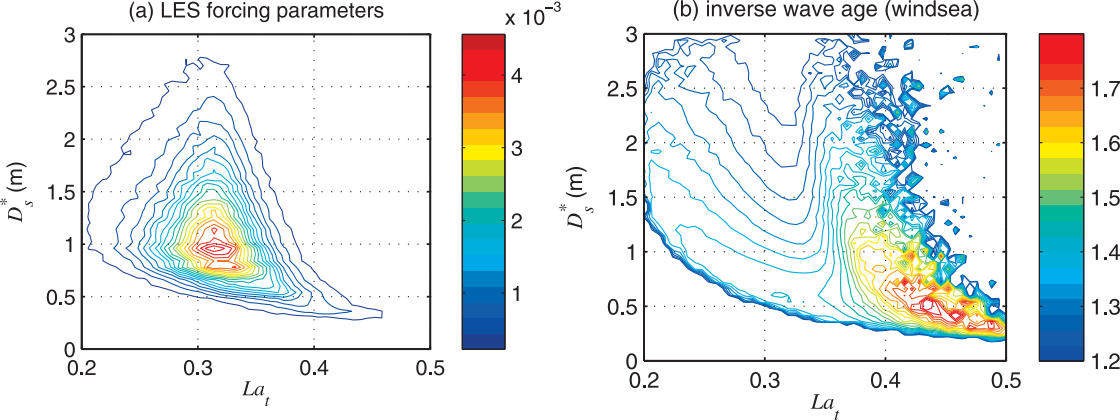
(a) LES forcing parameters
x 10^-3
4
3
2
1
3
2.5
2
1.5
1
0.5
0
0.2
0.3
0.4
0.5
D_s^* (m)
La_t
(b) inverse wave age (windsea)
1.7
1.6
1.5
1.4
1.3
1.2

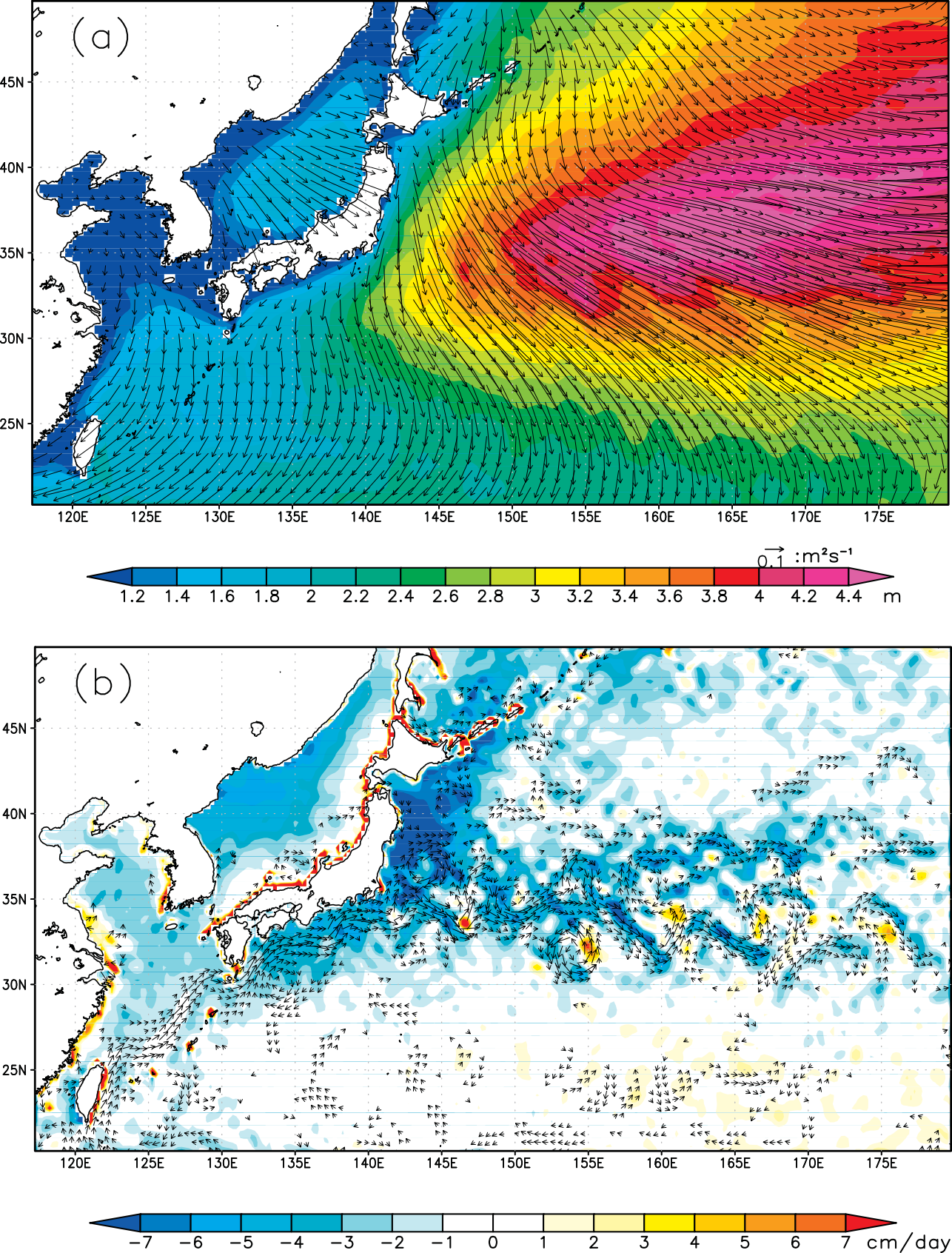
(a)
45N
40N
35N
30N
25N
120E
125E
130E
135E
140E
145E
150E
155E
160E
165E
170E
175E
0.1 :m²s⁻¹
1.2 1.4 1.6 1.8 2 2.2 2.4 2.6 2.8 3 3.2 3.4 3.6 3.8 4 4.2 4.4 m
(b)
45N
40N
35N
30N
25N
120E
125E
130E
135E
140E
145E
150E
155E
160E
165E
170E
175E
−7 −6 −5 −4 −3 −2 −1 0 1 2 3 4 5 6 7 cm/day

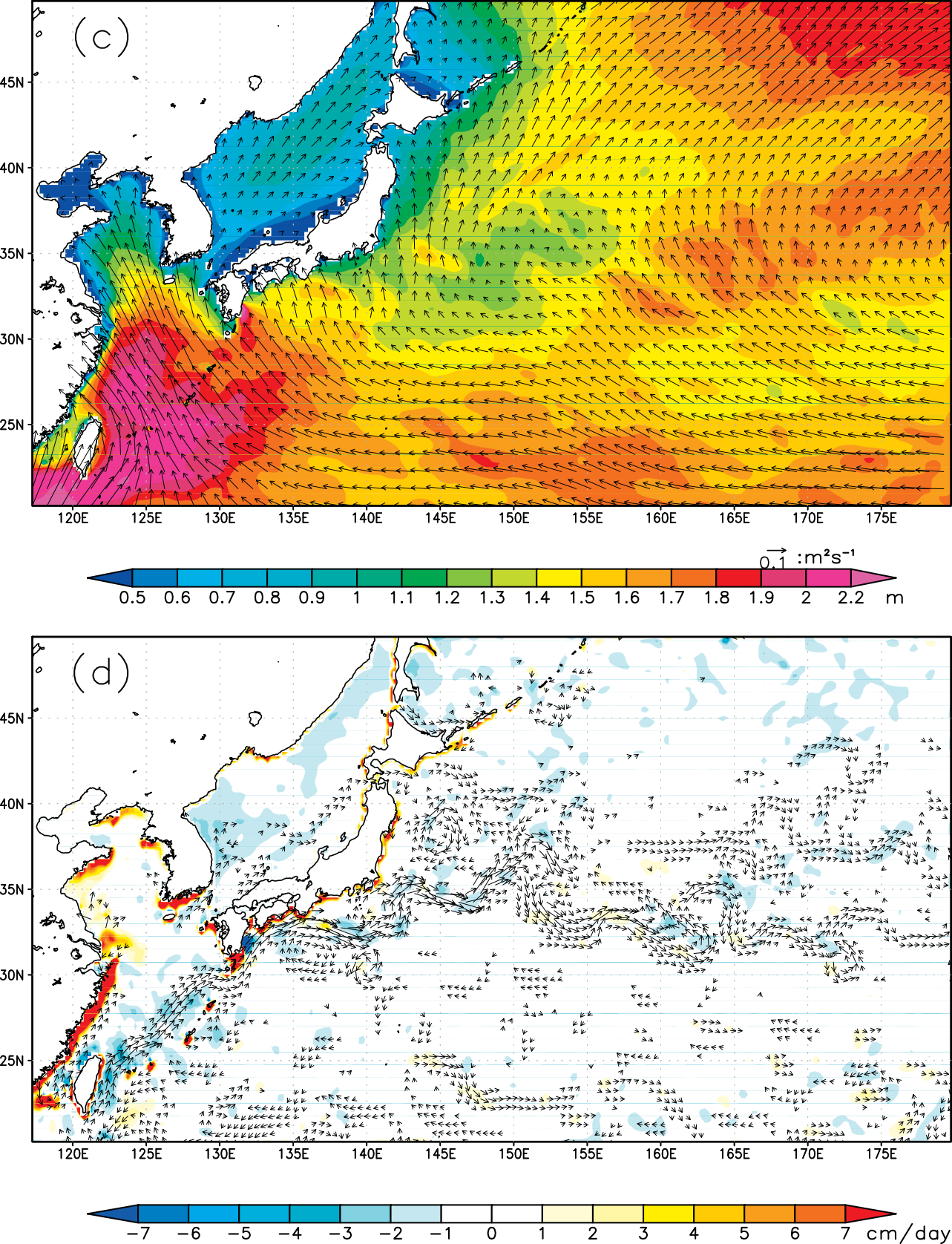
(c)
45N
40N
35N
30N
25N
120E
125E
130E
135E
140E
145E
150E
155E
160E
165E
170E
175E
0.1 :m²s⁻¹
0.5 0.6 0.7 0.8 0.9 1 1.1 1.2 1.3 1.4 1.5 1.6 1.7 1.8 1.9 2 2.2 m
(d)
45N
40N
35N
30N
25N
120E
125E
130E
135E
140E
145E
150E
155E
160E
165E
170E
175E
−7 −6 −5 −4 −3 −2 −1 0 1 2 3 4 5 6 7 cm/day

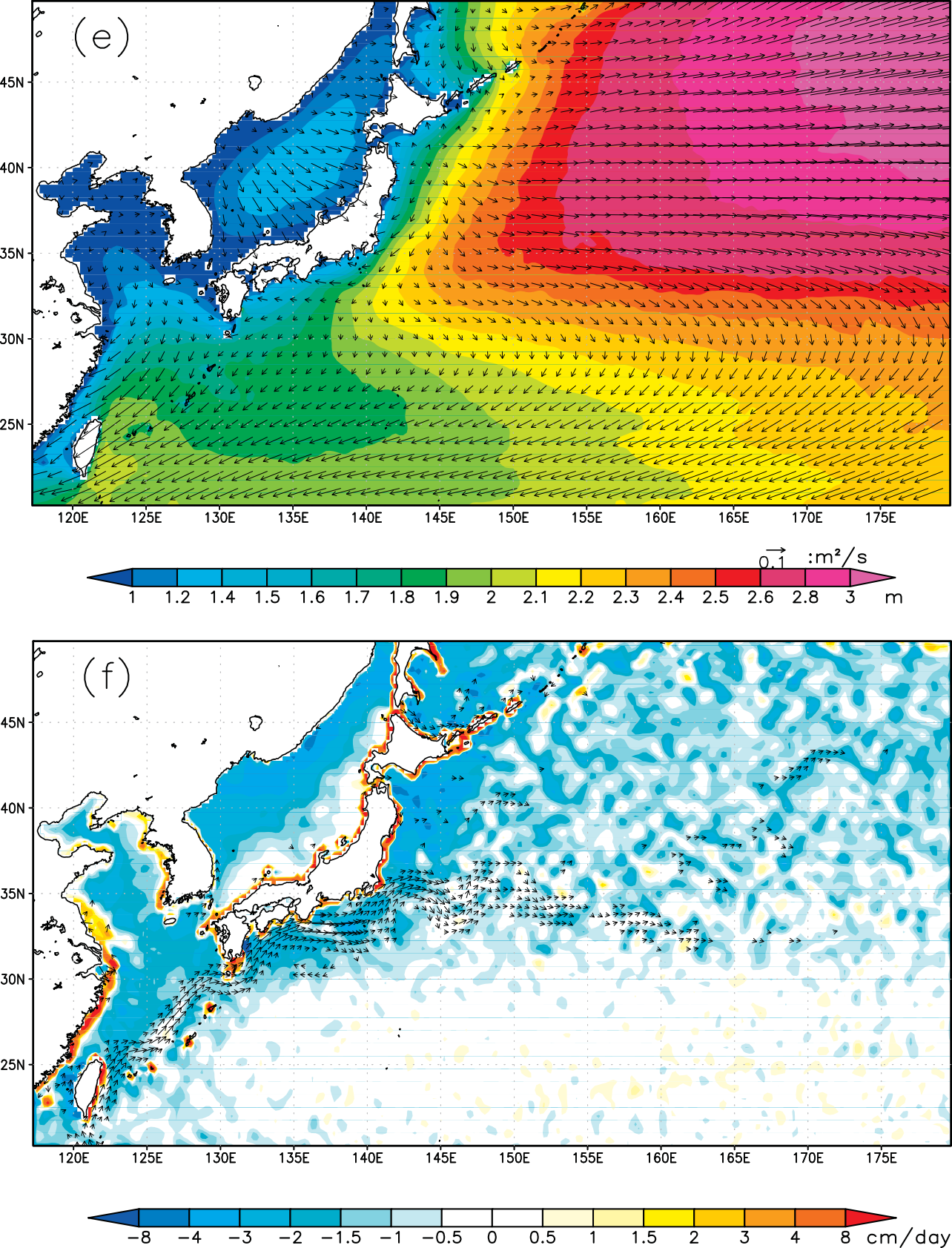
(e)
45N
40N
35N
30N
25N
120E
125E
130E
135E
140E
145E
150E
155E
160E
165E
170E
175E
0.1 :m²/s
1 1.2 1.4 1.5 1.6 1.7 1.8 1.9 2 2.1 2.2 2.3 2.4 2.5 2.6 2.8 3 m
(f)
45N
40N
35N
30N
25N
120E
125E
130E
135E
140E
145E
150E
155E
160E
165E
170E
175E
−8 −4 −3 −2 −1.5 −1 −0.5 0 0.5 1 1.5 2 3 4 8 cm/day

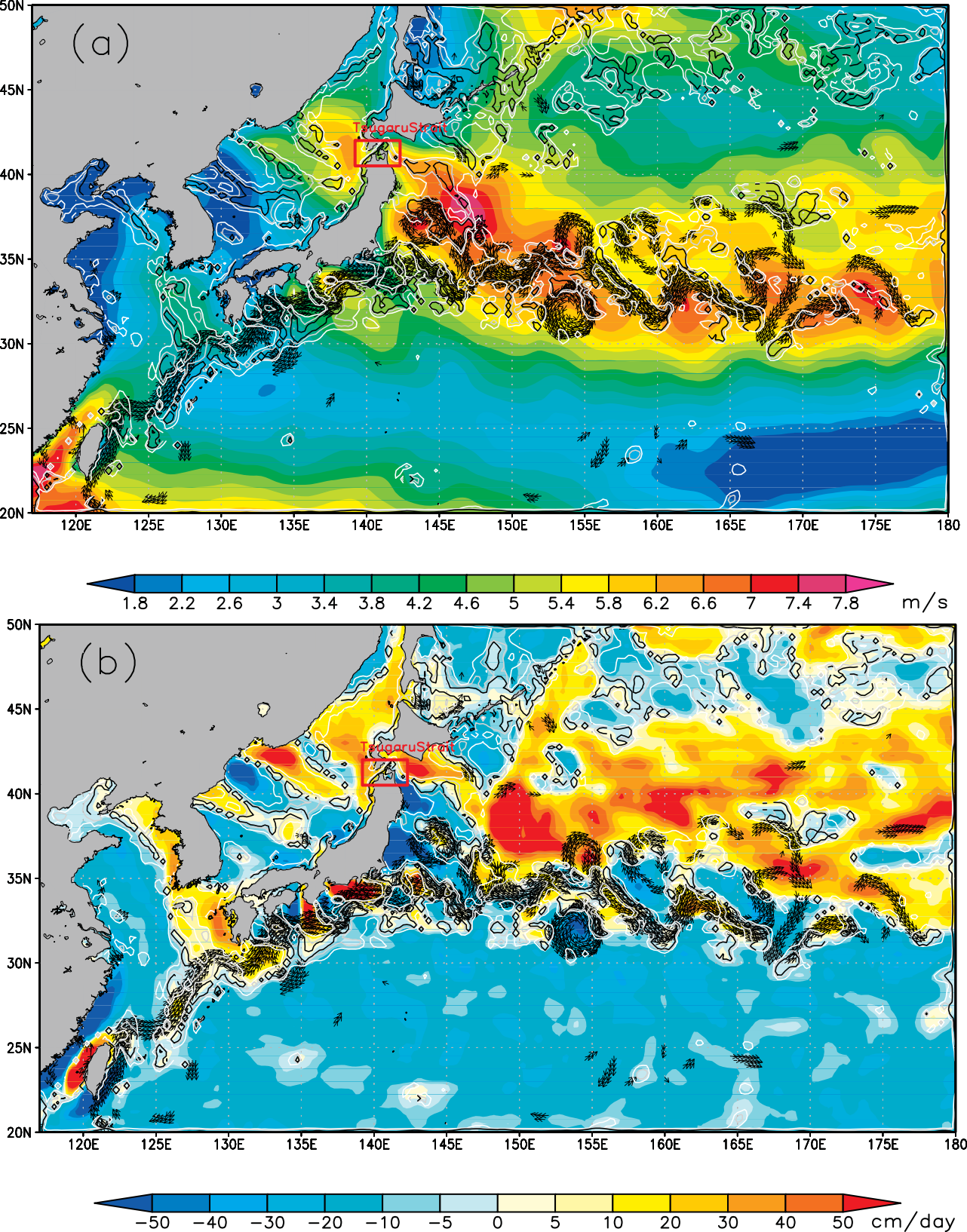
(a)
TsugaruStrait
50N
45N
40N
35N
30N
25N
20N
120E
125E
130E
135E
140E
145E
150E
155E
160E
165E
170E
175E
180
1.8 2.2 2.6 3 3.4 3.8 4.2 4.6 5 5.4 5.8 6.2 6.6 7 7.4 7.8
m/s
(b)
TsugaruStrait
50N
45N
40N
35N
30N
25N
20N
120E
125E
130E
135E
140E
145E
150E
155E
160E
165E
170E
175E
180
−50 −40 −30 −20 −10 −5 0 5 10 20 30 40 50
cm/day

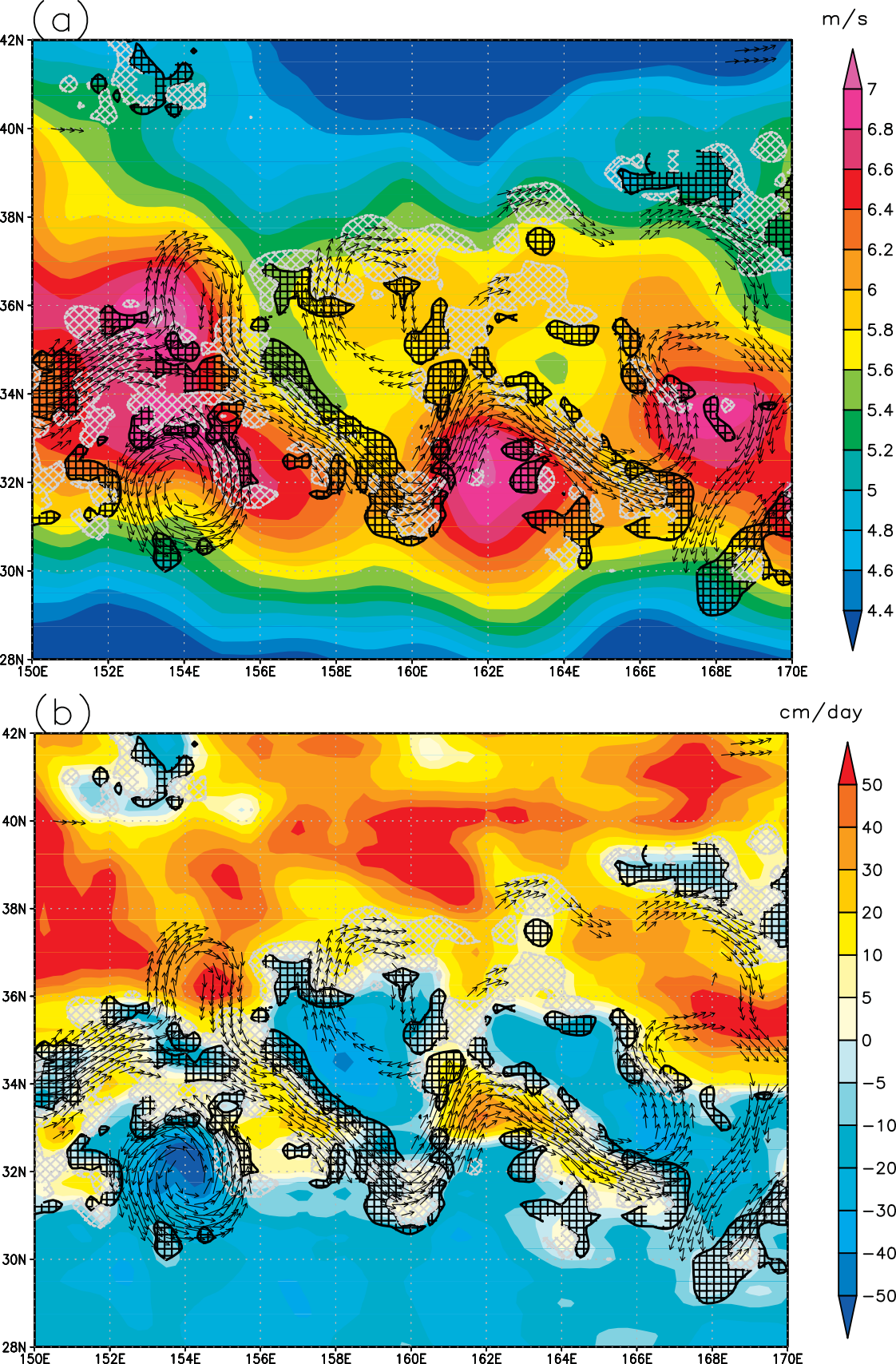
(a)
m/s
7
6.8
6.6
6.4
6.2
6
5.8
5.6
5.4
5.2
5
4.8
4.6
4.4
42N
40N
38N
36N
34N
32N
30N
28N
150E
152E
154E
156E
158E
160E
162E
164E
166E
168E
170E
(b)
cm/day
50
40
30
20
10
5
0
−5
−10
−20
−30
−40
−50
42N
40N
38N
36N
34N
32N
30N
28N
150E
152E
154E
156E
158E
160E
162E
164E
166E
168E
170E